Published in final edited form as:
Circ Res. 2006 April 14; 98(7): 879–886.

Emerging Imaging Techniques

Elliot R. McVeigh
From the Laboratory of Cardiac Energetics, NHLBI, National Institutes of Health, Bethesda, Md.

Abstract

This article reviews recent developments in selected imaging technologies focused on the cardiovascular system. The techniques covered are: ultrasound biomicroscopy (UBM), microSPECT, microPET, near infrared imaging, and quantum dots. For each technique, the basic physical principles are explained and recent example applications demonstrated.

Keywords

imaging; microPET; microSPECT; near infrared imaging; quantum dots; ultrasound imaging

Imaging technology has developed very rapidly over the past decade. In particular, the application of imaging to basic research in medical sciences have moved much of our understanding of cellular and molecular mechanics from the realm of inferred understanding to that of direct observation.[1-3] Much of the development has been in response to the need to image the genotype–phenotype relationship in genetically altered mice.[4,5] To perform longitudinal studies in which the development of genotypic features are tracked in the living organism, fast, high-resolution nondestructive imaging methods have been developed that are “tuned” specifically for imaging small animals such as mice.[6-8] By using each animal as its own control, hypotheses about the onset of disease and the effectiveness of treatment can be tested with many fewer animals than would be required with terminal studies.

In this review, a selected group of imaging methods are reviewed that span preclinical applications in small animals through methods available for patients today. The common theme among the methods described is that exciting new images are produced that have the potential to advance our understanding of cardiovascular disease. Unfortunately, many exciting methods are not discussed, such as bioluminescence,[9] intravascular ultrasound,[10] targeted microbubbles,[11] optical coherence tomography,[12] microCT from vendors such as: SCANCO Medical AG (Switzerland); GE Medical Systems, (Wakeshau Wis); and CTI Molecular Imaging (Knoxville, Tenn).[13] Their omission is simply because of a lack of space.

A recent trend in the development of imaging methods is to move traditional medical imaging techniques into the realm of laboratory science by simply increasing the spatial resolution achievable. This increase in spatial resolution does not come without a cost; usually, the field of view of the image must be decreased, and often the radiation dose is prohibitively high for work in live subjects. Microscopic magnetic resonance imaging (MRI) of samples in vitro has a long history,[14,15] as does high resolution computed tomography (CT) of materials.[16] Positron emission tomography (PET) is particularly suited for high-resolution in vivo imaging because it has such high tracer detection sensitivity; thus, very small numbers of cells or very low concentrations of tracer can be detected.

Correspondence to Elliot McVeigh, National Institutes of Health, DHHS, 10 Center Drive, Building 10, Room B1D416, Bethesda, MD 20892-1061. E-mail emcveigh@nih.gov

Ultrasound Biomicroscopy

The ability to increase the spatial resolution of ultrasound imaging with higher frequency transducers is not a new idea. High-frequency transducers have been used for such applications as dermatological imaging[17] and intravascular imaging.[10,18,19] High-frequency ultrasound imaging also holds promise for assessing microvascular blood flow in vivo. With frequencies in the range of 20 to 60 MHz, the imaging resolution is improved sufficiently to reconstruct dynamic signals from cylindrical volumes on the order of 43 μm diameter and 66 μm depth, over a field of view of 10 mm (width) and 5 mm (depth). This increased resolution is obtained by the design of high-frequency transducers.[20] These new systems have the ability to follow branching patterns of closely spaced microvessels from 30 μm to 100 μm in diameter.

Physical Principles of Ultrasound Biomicroscopy

The basic principle of ultrasound imaging is the detection of features within the body as reflecting surfaces for the sound waves transmitted from an oscillating transducer pressed up against the body surface. If high frequency sound waves are used, the wavelengths are shorter yielding a more precise estimate of the distances between reflecting surfaces. One implementation of a high-resolution ultrasound imaging system consists of a 3-dimensional micropositioning scanhead that rasters a transducer over the imaging field (8 mm×8 mm).[21,22] Ultrasound data are collected at equally spaced lines in steps of 10 to 20 μm between each line. The selectable frequency range of the scanner (19 to 55 MHz) corresponds to maximum imaging depths of ≈15 mm and 5 mm, respectively. The standard transducer used on a specially designed “mouse imager” is a 3-mm diameter 40-MHz center frequency device with a focal length of 6 mm.

For imaging vascular flow, pulsed Doppler processing is used. The ultrasound image is used to identify vessels or cardiac structures. A sample volume is placed interactively by the user on the target structure and the pulsed Doppler system returns the Doppler waveform for that location (after angle correction). The minimum detectable velocity depends on: the Doppler angle, the ratio of blood scatter to tissue scatter, clutter arising from tissue motion, and signal sampling as dictated by the pulse-repetition frequency. The minimum detectable velocity of the mouse imaging system is ≈1 mm/s, consistent with blood velocities in the microcirculation.

Applications of Ultrasound Biomicroscopy

An example application of the in vivo ultrasound biomicroscopy is shown in Figure 1a, where images of a developing mouse heart obtained in utero are shown with the corresponding one-dimensional Doppler flow spectra. The images in Figure 1b show the system used for a comprehensive transthoracic cardiac examination in the mouse with anatomical confirmation by MRI.[21,23] The obvious next step in the development of this imaging method is a true phased array transducer that is capable of performing the “raster” by focusing the beam rapidly across the sample as is currently performed in clinical ultrasound systems. Future applications could include dynamic imaging of vessel wall morphology, longitudinal studies of plaque formation, and real-time guidance of microsurgical interventions in small animals.

Single Photon Emission Tomography for Small Animal Imaging (microSPECT)

Physical Principles of SPECT

In SPECT imaging, a radionuclide tracer is injected into the blood. It accumulates at different locations in the body depending on the relative perfusion and affinity for the compound containing the radionuclide. The SPECT camera then estimates the relative amount of activity at each position in the body by detecting the emission of gamma rays from a series of angular views. The resolution of the resulting image is dependent on the aperture through which the radiation is detected.

For SPECT studies in small experimental animals, the risk of radiation dose is not a significant issue; therefore, increased resolution in the imaging system can be achieved through drastic collimation, such as a pin-hole collimator, which limits each view of the gamma camera to a precise line through the animal. Weber et al[24-26] have been developing pinhole SPECT systems for over a decade. Also, a cylindrical fixed camera systems with multiple pin-holes has been developed.[27] For this system, there is no need to correct for the center of rotation of the SPECT camera head, and there is obviously better efficiency at capturing the gamma radiation emitted from the subject. This system has recently been shown to accurately images myocardial infarcts in the rat model as shown in Figure 2.[28]

The FASTSPECT system[27-29] comprises two circular arrays of modular gamma cameras. One array has 11 cameras and the other array has 13 cameras. Each modular camera consists of a 10×10 cm NaI(Tl) scintillation crystal (Rexon Components, Inc, Beachwood, Ohio), with an optical light guide leading to four (5×5 cm) photomultiplier tubes (Hamamatsu Photonics K.K., Hamamatsu, Japan). Twenty-four 1-mm–diameter pin-holes are drilled in the cylindric aperture; a point source in the center of the field of view was simultaneously projected to the center of each camera. The field of view of the system is 3.0×3.2×3.2 cm and the magnification is a factor of 3.5. The spatial resolution is 1.5 mm, and the sensitivity of the system for a point source in air is 13.3 cps/microCi (0.359 cps/kBq). The benefit of this fixed detector system is that no motion by the aperture or detector is required for acquisition of projection data. Artifacts caused by detector motion or aperture structure are therefore avoided.

Applications of microSPECT

SPECT can be used to determine the region of myocardium at risk by performing a ^{99m}TC-sestamibi injection during coronary ligation, showing the region of reduced blood flow. The resultant size of the infarct can be determined by injection of ^{99m}Tc-sestamibi after release of the ligation. The case in which the ^{99m}Tc-sestamibi is not taken up by the cells corresponds to infarcted tissue. This particular application has been demonstrated by Liu et al.[28]

Liu and colleagues showed that the high-resolution fixed detector SPECT system was able to delineate infarct sizes in the rat myocardium with a very high correlation to the TTC staining of those regions. These rats had undergone left coronary ligation for 90 minutes, followed by 30 minutes of reperfusion before an injection of 5 to 10 mCi ^{99m}Tc-sestamibibi into the femoral vein. This creates the possibility of serial imaging of rats that have undergone revascularization therapy, or the evaluation of myocardial protection with drugs. Figure 2 shows a comparison of the SPECT images from four slices versus both the Evans blue and TTC stained slices. The spatial resolution of the SPECT images is clearly sufficient to image the ischemic zone with high precision. Recently, the system has been used with ^{99m}Tc-glucarate for sizing myocardial infarcts and measuring differences in washout kinetics depending on the severity of the infarct.[29] The future applications of microSPECT could include serial imaging of infarcts to measure the evolution of the injury zone during different treatment regimes, and gated blood pool studies to acquire simultaneous estimates of ventricular function. Future application of gated studies will also decrease the effect of cardiac motion on the images of the infarction.

PET for Small Animal Imaging (microPET)

PET is a well-established imaging method used to map the distribution of injected radiolabeled tracers within a living organism. PET has been used extensively for imaging cancer, neurological function, and cardiovascular disease.[30] The recent interest in imaging genetically altered mice has lead to the development of high-resolution PET scanners custom designed for small animal imaging.[31-34]

Physical Principles of PET

The advantage of PET over SPECT is the improved resolution due to the natural “collimation” provided by the physics. In PET, a “count” is recorded when *two* 511KeV gamma rays *simultaneously* trigger detectors on opposite sides of the sample. The line drawn through space between the two detectors gives the only possible locus of points from which the annihilation event could occur releasing the two gamma rays in opposite directions; thus, effective collimation is achieved. The creation of positron emitters that attach to biologically active molecules allows PET to probe the functional biochemistry of the living organism.

Imaging System Design

Tai et al have recently described a new high resolution PET designed to image small animals. This system uses for its detectors 14×14 grids of lutetium oxyorthosilicate crystals spaced at 1.15-mm spacings. Each of these detectors is arranged 3-deep in a ring that has a diameter of 16 cm (30 detectors circumferentially ×3 axially), with a 4.9-cm field of view (FOV) in the axial direction. The details of the system are given in reference [34].

The image resolution of this scanner was measured with a 0.5-mm small source, moved to different offsets from the center of the field of view. At the center the resolution (full width at half max) was (0.86 mm×0.83 mm×1.25 mm, (*radial×tangential×axial directions*), whereas at a radial offset of 2 cm the resolution was (1.97 mm×1.22 mm×1.50 mm). The volumetric image resolution was found to depend strongly on the reconstruction algorithm used and averaged 1.1 mm (1.4 μL) across the central 3 cm of the transaxial FOV when using a statistical reconstruction algorithm with accurate system modeling.[35,36] It was found that different scanner settings were required for different sized animal (ie, mouse versus rat).[37]

Applications of microPET

The imaging of gene expression is of particular interest with the recent developments of localized genetic therapies for the treatment of ischemia and infarction.[38-41] Gambhir and colleagues have demonstrated the ability to image local expression of a herpes simplex virus type 1 mutant thymidine kinase (HSV1-sr39tk) as a PET reporter gene using 9-(4-[18F]-fluoro-3 hydroxymethylbutyl) guanine ([18F]-FHBG) as a PET reporter probe in the rat heart.[42,43] The HSV1-sr39tk gene encodes for a mutant thymidine kinase enzyme that phosphorylates and accumulates [18F]-FHBG inside the cell. Using a microPET system for small animals this accumulation can be localized and quantified.

Figure 3 shows microPET images of a rat 4 days after the intramyocardial injection of Ad-CMV-HSV1-sr39tk. There is focal cardiac [18F]-FHBG activity at the site of injection, and this activity is well-localized when superimposed on the [13N]-NH3 grayscale images. Using microPET, the level of expression can be quantified in serial studies in the same animals.[44] This has obvious implications for the development and tuning of expression profiles in genetic therapy.

For this particular application, PET offers a distinct sensitivity advantage over other imaging methods. PET has extremely high sensitivity and can therefore resolve very small numbers of reporter probes (10^{-12} mol/L). This is important for imaging agents that have low transduction efficiency or for gene delivery vectors that have weak promoters.

PET will always be helped by a well-registered anatomical image to pinpoint the location of the activation measured with the PET detector. Secondly, precise attenuation correction in the

PET reconstruction algorithm can be incorporated using CT images. This has lead to the development of co-linear PET/CT scanners, which are commercially available.[45] Such systems and PET/MRI counterparts will likely be essential in answering important questions about the relationship of recovered function to local therapy delivery. For example, with PET/MRI co-registered data it would be possible to measure the local increase in function at locations of stem cell homing.

Near Infrared Fluorescence Imaging

Physical Principles of Near Infrared Imaging

Fluorescent dyes are a mainstay for isolating structures in modern optical microscopy. Fluorescent dyes can also be used as a contrast agent in optical imaging to make selected structures, such as vessels, “glow” in a dark background. Near Infrared (NIR) (700 to 1000 nm) light has been used for biomedical imaging due to the relatively low absorption of hemoglobin (Hb) and water at these wavelengths. Development of contrast agents that fluoresce in this range allows real-time imaging of both morphology and function of the tissue. Frangioni and colleagues have developed a method for obtaining images of vessels and myocardial perfusion after the injection of NIR fluorophores on the exposed surface of the heart.[46-48] In this way, the advantages of improved depth of penetration for IR versus visible light are achieved while using an agent to isolate morphology such as vessels, and measure physiological function, such as perfusion.

Imaging System Design

In this imaging method the heptamethine indocyanine-type NIR fluorophores IR-786, and the carbolylic acid from of IRDye78 (IRDye78-CA) were injected intravenously as perfusion and intravascular contrast agents respectively. The IR-786 partitions into mitochondria and endoplasmic reticulum and is thus used as a marker of tissue perfusion. The IRDye78-CA is a highly charged derivative of IR-786 that can be used to visualize the vessels. No apparent acute toxicity was observed with these agents at the doses required to visualize function; however, at high doses IR-786 may have caused arrhythmia during ischemia.

NIR excitation was via a custom 771 nm, 250 mW laser diode system at a fluence rate of 50 mW/cm^2. White light excitation was via a 150 mW halogen lamp, depleted of wavelengths >700 nm. An Orca ER NIR camera was used to obtain a 640×480 pixel field of view.

Applications of NIR Fluoroscopic Imaging

The principal application for this imaging technique is intraoperative visualization of blood flow and perfusion. Figure 4 shows an example from Nakayama et al[47] of intraoperative imaging of flow and perfusion deficits after prolonged ischemia (30 minutes of left anterior descending [LAD] vessel ligation).

Taggart and colleagues have used a commercially developed NIR imaging system (Novadaq Technologies, Toronto, Canada) to detect early graft failure after coronary artery bypass grafting in humans.[49] This is a common cause of morbidity and mortality and is of particular concern in off-pump coronary artery bypass grafting.

The SPY system by Novadaq is based on fluorescence of Indocyanine Green when exposed to near infrared light after a direct 1-mL bolus venous injection. The vessels stand out in stark contrast to the background tissue and the images can be used to monitor the existence of flow in real-time. The usefulness of this method was demonstrated by the detection of graft failure in 5% of patients who were studied; surgical revision to correct the graft was undertaken in these cases. Figure 5 shows an example of an anastomosis that had to be taken down and reconstructed when it was discovered that flow to the distal LAD was impeded. It is clear that this technology will have applications in many vascular surgical applications outside the heart. Also, the ability to monitor the change in perfusion during the procedure allows investigators to probe precise relationships between perfusion deficits and electrical function of the myocardium with mapping techniques.

Near Infrared Spectroscopic Imaging

Physical Principles of NIR spectroscopic imaging

Near-infrared spectroscopy has been used for a long time to measure blood oxygenation, usually in a fingertip, or an earlobe. A source of light at two wavelengths, say 650 nm and 805 nm, is used to illuminate a volume of tissue. The amount of absorption of the light at each frequency is dependent on the level of oxygen saturation of the hemoglobin in the blood because of the different absorption spectra of oxygenated hemoglobin (oxy-Hb) and deoxygenated hemoglobin. The simple two-point estimate of the absorption spectrum is enough to obtain the level of oxygenation.

Nighswander-Rempel and colleagues[50] have proposed a method for obtaining spatially localized estimates of blood oxygenation using imaging. Similarly, Torricelli and colleagues have measured calf muscle oxygenation and hemoglobin content during exercise.[51]

Imaging System Design

To make maps of the relative IR absorption spectra, a simple camera imaging system can be used. In the approach used by Nighswander-Rempel et al[50] an IR-sensitive 512×512 back-illuminated charged coupled device element and 14/16-bit ST-138 analog to digital converter run in 14-bit mode (Princeton Instruments, Trenton, NJ) were used with a Nikon Micro AF60 lens to make a 2D IR “spectral camera.” To sample different spectral bands of 7-nm width, a liquid crystal tuneable filter (Cambridge Research Instruments, Woburn, Mass) was mounted to the camera lens, providing an adjustable passband between 650 and 1050 nm. By scanning through different wavelengths, a 3-dimensional image can be reconstructed with spatial coordinates in two dimensions and spectral information in the third dimension. Using the spectral information, images can be computed that are maps depicting the relative concentrations of deoxy-(Hb+Mb) and oxy-(Hb+Mb) at each point in the entire heart. (Mb is myoglobin, spectrally indistinguishable from hemoglobin).

Applications of NIR Spectroscopic Imaging

To demonstrate the ability of the system to image the oxygenation state of cardiac tissue, isolated pig hearts were imaged before and during occlusion of the left anterior descending artery. The hearts were illuminated with quartz halogen floodlights. NIR reflectance images were acquired from a reference standard (Kodak Gray Card) and also from the exposed surface of the heart. The spectroscopic images were created from 41 individual 10-nm band images between 650 and 1050 nm. The acquisition of the image over the entire spectrum took 5 minutes.

Figure 6a shows changes in the deoxy(Hb−Mb) concentration for three tissue states: normal perfusion, during LAD occlusion, and during recovery. The region of high deoxy(Hb−Mb) is highlighted extremely well. In Figure 6b the decrease in oxy(Hb−Mb) is shown during the same perfusion states as Figure 6a. It is envisioned that this type of image will be useful in the operating room during revascularization to get a precise, quantitative measurement of the effect of the renewed blood flow.

Quantum Dots

Imaging fluorophores in the cell has been the major advance in biological microscopy in the past 20 years. Whereas a number of techniques use the property of photobleaching to tag populations of fluorophores in the cell, photobleaching also limits the amount of imaging that can be performed. Imaging multiple fluorophores in a single sample can be difficult due to the requirement for an individual excitation for each fluorophore and the existence of overlapping emission spectra from the multiple fluorophores. The recent introduction of inorganic fluorophores, which are small semiconductor crystals called quantum dots (QDs), has provided a new source of fluorescence without these limitations.[52-54] These are now commercially available from companies such as Quantum Dot Corp (Hayward, Calif).

Physical Principles of QDs

QDs are semiconductor crystals that range in size from 2 to 5 nm in diameter (approximately the same size as Green Fluorescent Protein). The emission spectrum of the QD is determined by its diameter; the larger the QD, the longer the wavelength of the emission. The excitation spectrum of these QDs is very broad, and the emission spectrum has a relatively narrow full width at half max of 20 to 40 nm. Almost the entire emission spectrum can be collected, due to the fact that the overlap with the excitation spectrum is small. Also, QDs are able to fluoresce for many *hours* under constant 50 mW excitation, whereas organic fluorophores photobleach after tens of minutes under the same exposure. Because QDs are not susceptible to chemical degradation in the cell, they can be used to label cells for longitudinal studies, and multiple species of QDs can be imaged simultaneously. They have been shown to remain fluorescent for up to 4 months in vivo.[55]

Applications of QDs

Whole body images of 6- to 12-week-old nude mice were obtained by illuminating the animal with 200 W excitation after a tail vein injection of QDs conjugated with methoxy- or carboxy-terminated poly(ethylene glycol) amine (mPEG-750 QDs) at the concentration of 20 pmol/g (animal weight).[55] Bandpass filters of 20 nm were used to collect images for 200 ms through 5 s to bracket the dynamic range of intensities. A sample image 1 minute after injection of the mPEG-750 QDs is shown in Figure 7.

Water-soluble cadmium selenide–zinc sulfide QDs have been used as a fluorescence angiography probe by imaging capillaries deep within the skin of the mouse with multi-photon excitation after a tail vein injection.[56] The vessels were clearly depicted hundreds of microns deep below the skin surface. High resolution line scans across these capillaries were used to measure capillary flow to be ≈10 μm/s. This is shown in Figure 8.

Toward immunohistochemical applications, ZnS-capped CdSe QDs have been conjugated to streptavidin and a mono-clonal anti-body for the CA125 antigen in cellular and whole tissue samples.[57] Also, to test the effect of QD labeling on cell behavior, Voura et al[58] injected tumor cells labeled with QDs into mice, and the extravasation of those cells into lung tissue was measured. The cells labeled with the QD behaved precisely the same as the cells without the QD particles. In addition, five different populations of cells labeled with different QDs were tracked simultaneously. Recently, Kim et al have shown the use of water soluble NIR QDs for marking lymph nodes to be resected.[59] Morgan et al have shown NIR QDs for real-time angiographic imaging and pharmacokinetics in the mouse.[60]

The challenges that lie ahead for using QDs to track individual cells is the conjugation of the QDs with a host of biological molecules[61] and the efficient introduction of the QDs into cells.

Summary

Although a relatively limited number of cardiovascular imaging applications were covered in this article, it is clear that the technology in this field continues to develop at an ever-increasing pace. With the advent of new contrast agents, such as fluorophores, QDs, and PET tracers, the techniques described herein will become an essential part of the experimental cardiovascular laboratory.

Acknowledgments

This work was supported by the intramural research program of the National Institutes of Health and National Heart Lung and Blood Institute. The author thanks those who permitted the use of figures for this article. Those authors are cited in the figure captions and permission was granted from the respective publishers.

References

1. Mountz JD, Hsu HC, Wu Q, Liu HG, Zhang HG, Mountz JM. Molecular imaging: new applications for biochemistry. J Cell Biochem Suppl 2002;39:162–171. [PubMed: 12552616]
2. Heckl S, Pipkorn R, Nagele T, Vogel U, Kuker W, Voight K. Molecular imaging: Bridging the gap between neuroradiology and neurohistology. Histol Histopathol 2004;19:651–668. [PubMed: 15024722]
3. Brown FD, Rozelle AL, Yin HL, Balla T, Donaldson JG. Phosphatidylinositol 4,5-bisphosphate and Arf6-regulated membrane traffic. J Cell Biol 2001;154:1007–1017. [PubMed: 11535619]
4. Chien KR. Genes and physiology: molecular physiology in genetically engineered animals. J Clin Invest 1996;97:901–909. [PubMed: 8613542]
5. Christensen G, Wang Y, Chien KR. Physiological assessment of complex cardiac phenotypes in genetically engineered mice. Am J Physiol 1997;272:H2513–H2524. [PubMed: 9227526]
6. Budinger TF, Benaron DA, Koretsky AP. Imaging transgenic animals. Annu Rev Biomed Eng 1999;1:611–648. [PubMed: 11701502]
7. Stout DB, Chatziioannou AF, Lawson TP, Silverman RW, Gambhir SS, Phelps ME. Small Animal Imaging Center Design: The Facility at the UCLA Crump Institute for Molecular Imaging. Mol Imaging Biol 2005:1–10. [PubMed: 15912268]
8. Nieman BJ, Bock NA, Bishop J, Chen XJ, Sled JG, Rossant J, Henkelman RM. Magnetic resonance imaging for detection and analysis of mouse phenotypes. NMR Biomed 2005;18:447–468. [PubMed: 16206127]
9. Weissleder R, Ntziachristos V. Shedding light onto live molecular targets. Nat Med 2003;9:123–128. [PubMed: 12514725]
10. Schoenhagen P, Nissen S. Understanding coronary artery disease: tomographic imaging with intravascular ultrasound. Heart 2002;88:91–96. [PubMed: 12067962]
11. Lindner JR. Microbubbles in medical imaging: current applications and future directions. Nat Rev Drug Discov 2004;3:527–532. [PubMed: 15173842]
12. Brezinski M. Characterizing arterial plaque with optical coherence tomography. Curr Opin Cardiol 2002;17:648–655. [PubMed: 12466708]
13. Ritman EL. Micro-computed tomography-current status and developments. Annu Rev Biomed Eng 2004;6:185–208. [PubMed: 15255767]
14. Johnson GA, Cofer GP, Gewalt SL, Hedlund LW. Morphologic phenotyping with MR microscopy: the visible mouse. Radiology 2002;222:789–793. [PubMed: 11867802]
15. Johnson GA, Benveniste H, Engelhardt RT, Qiu H, Hedlund LW. Magnetic resonance microscopy in basic studies of brain structure and function. Ann N Y Acad Sci 1997;820:139–147. [PubMed: 9237453]
16. Finnigan P, Hathaway A, Lorensen W, Connell I, Paschal CB, Ross J. CATFEM - Computer-Assisted Tomography and Finite Element Modeling. Control and Dynamic Systems 1991;49:289–337.
17. Jemec GB, Gniadecka M, Ulrich J. Ultrasound in dermatology. Part I. High frequency ultrasound. Eur J Dermatol 2000;10:492–497. [PubMed: 10980479]

18. Nissen SE, Yock P. Intravascular ultrasound: novel pathophysiological insights and current clinical applications. Circulation 2001;103:604–616. [PubMed: 11157729]

19. Nissen SE. Application of intravascular ultrasound to characterize coronary artery disease and assess the progression or regression of atherosclerosis. Am J Cardiol 2002;89:24B–31B.

20. Foster FS. Transducer materials and probe construction. Ultrasound Med Biol 2000;26(Suppl 1):S2–S5. [PubMed: 10794861]

21. Zhou YQ, Foster FS, Nieman BJ, Davidson L, Chen XJ, Henkelman RM. Comprehensive transthoracic cardiac imaging in mice using ultrasound biomicroscopy with anatomical confirmation by magnetic resonance imaging. Physiol Genomics 2004;18:232–244. [PubMed: 15114000]

22. Foster FS, Zhang M, Duckett AS, Cucevic V, Pavlin CJ. In vivo imaging of embryonic development in the mouse eye by ultrasound biomicroscopy. Invest Ophthalmol Vis Sci 2003;44:2361–2366. [PubMed: 12766031]

23. Zhou YQ, Zhu Y, Bishop J, Davidson L, Henkelman RM, Bruneau BG, Foster FS. Abnormal cardiac inflow patterns during postnatal development in a mouse model of Holt-Oram syndrome. Am J Physiol Heart Circ Physiol 2005;289:H992–H1001. [PubMed: 15849237]

24. Weber DA, Ivanovic M, Franceschi D, Strand SE, Erlandsson K, Franceschi M, Atkins HL, Coderre JA, Susskind H, Button T. Pinhole SPECT: an approach to in vivo high resolution SPECT imaging in small laboratory animals. J Nucl Med 1994;35:342–348. [PubMed: 8295008]

25. Weber DA, Ivanovic M. Pinhole SPECT: ultra-high resolution imaging for small animal studies. J Nucl Med 1995;36:2287–2289. [PubMed: 8523121]

26. Weber DA, Ivanovic M. Ultra-high-resolution imaging of small animals: implications for preclinical and research studies. J Nucl Cardiol 1999;6:332–344. [PubMed: 10385189]

27. Klein WP, Barrett HH, Pang IW, et al. FASTSPECT: electrical and mechanical design of a high resolution dynamic SPECT imager. IEEE Nuclear Science Symposium and Medical Imaging, San Francisco 1995;2:931–933.

28. Liu Z, Kastis GA, Stevenson GD, Barrett HH, Furenlid LR, Kupinski MA, Patton DD, Wilson DW. Quantitative analysis of acute myocardial infarct in rat hearts with ischemia-reperfusion using a high-resolution stationary SPECT system. J Nucl Med 2002;43:933–939. [PubMed: 12097466]

29. Liu Z, Barrett HH, Stevenson GD, Kastis GA, Bettan M, Furenlid LR, Wilson DW, Pak KY. High-resolution imaging with (99m)Tc-glucarate for assessing myocardial injury in rat heart models exposed to different durations of ischemia with reperfusion. J Nucl Med 2004;45:1251–1259. [PubMed: 15235074]

30. Phelps ME. PET. the merging of biology and imaging into molecular imaging. J Nucl Med 2000;41:661–681. [PubMed: 10768568]

31. Massoud TF, Gambhir SS. Molecular imaging in living subjects: seeing fundamental biological processes in a new light. Genes Dev 2003;17:545–580. [PubMed: 12629038]

32. Chatziioannou A, Tai YC, Doshi N, Cherry SR. Detector development for microPET II: a 1 microl resolution PET scanner for small animal imaging. Phys Med Biol 2001;46:2899–2910. [PubMed: 11720354]

33. Chatziioannou AF. Molecular imaging of small animals with dedicated PET tomographs. Eur J Nucl Med Mol Imaging 2002;29:98–114. [PubMed: 11807613]

34. Tai YC, Chatziioannou AF, Yang Y, Silverman RW, Meadors K, Siegel S, Newport DF, Stickel JR, Cherry SR. MicroPET II: design, development and initial performance of an improved microPET scanner for small-animal imaging. Phys Med Biol 2003;48:1519–1537. [PubMed: 12817935]

35. Qi J, Leahy RM, Cherry SR, Chatziioannou A, Farquhar TH. High-resolution 3D Bayesian image reconstruction using the microPET small-animal scanner. Phys Med Biol 1998;43:1001–1013. [PubMed: 9572523]

36. Chatziioannou A, Qi J, Moore A, Annala A, Nguyen K, Leahy R, Cherry SR. Comparison of 3-D maximum a posteriori and filtered backprojection algorithms for high-resolution animal imaging with microPET. IEEE Trans Med Imaging 2000;19:507–512. [PubMed: 11021693]

37. Yang Y, Tai YC, Siegel S, Newport DF, Bai B, Li Q, Leahy RM, Cherry SR. Optimization and performance evaluation of the microPET II scanner for in vivo small-animal imaging. Phys Med Biol 2004;49:2527–2545. [PubMed: 15272672]

38. de Vries EF, Vaalburg W. Positron emission tomography: measurement of transgene expression. Methods 2002;27:234–241. [PubMed: 12183112]
39. Nugent HM, Edelman ER. Tissue engineering therapy for cardiovascular disease. Circ Res 2003;92:1068–1078. [PubMed: 12775655]
40. Gambhir SS. Molecular imaging of cancer with positron emission tomography. Nat Rev Cancer 2002;2:683–693. [PubMed: 12209157]
41. Sun X, Annala AJ, Yaghoubi SS, Barrio JR, Nguyen KN, Toyokuni T, Satyamurthy N, Namavari M, Phelps ME, Herschman HR, Gambhir SS. Quantitative imaging of gene induction in living animals. Gene Ther 2001;8:1572–1579. [PubMed: 11704818]
42. Gambhir SS, Bauer E, Black ME, Liang Q, Kokoris MS, Barrio JR, Iyer M, Namavari M, Phelps ME, Herschman HR. A mutant herpes simplex virus type 1 thymidine kinase reporter gene shows improved sensitivity for imaging reporter gene expression with positron emission tomography. Proc Natl Acad Sci U S A 2000;97:2785–2790. [PubMed: 10716999]
43. Wu JC, Inubushi M, Sundaresen G, Schelbert HR, Gambhir SS. Positron emission technology imaging of cardiac reporter gene expression in living rats. Circulation 2002;106:180–183. [PubMed: 12105155]
44. Inubushi M, Wu JC, Gambhir SS, Sundaresan G, Satyamurthy N, Namavari M, Yee S, Barrio JR, Stout D, Chatziioannou AF, Wu L, Schelbert HR. Positron-emission tomography reporter gene expression imaging in rat myocardium. Circulation 2003;107:326–332. [PubMed: 12538436]
45. Townsend DW, Carney JP, Yap JT, Hall NC. PET/CT today and tomorrow. J Nucl Med 2004;45 (Suppl 1):4S–14S. [PubMed: 14736831]
46. Zaheer A, Lenkinski RE, Mahmood A, Jones AG, Cantley LC, Frangioni JV. In vivo near-infrared fluorescence imaging of osteoblastic activity. Nat Biotechnol 2001;19:1148–1154. [PubMed: 11731784]
47. Nakayama A, del Monte F, Hajjar RJ, Frangioni JV. Functional near-infrared fluorescence imaging for cardiac surgery and targeted gene therapy. Mol Imaging 2002;1:365–377. [PubMed: 12940233]
48. Frangioni JV. In vivo near-infrared fluorescence imaging. Curr Opin Chem Biol 2003;7:626–634. [PubMed: 14580568]
49. Taggart DP, Choudhary B, Anastasiadis K, Abu-Omar Y, Balacumaraswami L, Pigott DW. Preliminary experience with a novel intraoperative fluorescence imaging technique to evaluate the patency of bypass grafts in total arterial revascularization. Ann Thorac Surg 2003;75:870–873. [PubMed: 12645709]
50. Nighswander-Rempel SP, Anthony SR, Mansfield JR, Hewko M, Kupriyanov VV, Mantsch HH. Regional variations in myocardial tissue oxygenation mapped by near-infrared spectroscopic imaging. J Mol Cell Cardiol 2002;34:1195–1203. [PubMed: 12392893]
51. Torricelli A, Quaresima V, Pifferi A, Biscotti G, Spinelli L, Taroni P, Ferrari M, Cubeddu R. Mapping of calf muscle oxygenation and haemoglobin content during dynamic plantar flexion exercise by multi-channel time-resolved near-infrared spectroscopy. Phys Med Biol 2004;49:685–699. [PubMed: 15070196]
52. Watson A, Wu X, Bruchez M. Lighting up cells with quantum dots. Biotechniques 2003;34:296–293. [PubMed: 12613252]
53. Jaiswal JK, Simon SM. Potentials and pitfalls of fluorescent quantum dots for biological imaging. Trends Cell Biol 2004;14:497–504. [PubMed: 15350978]
54. Lim YT, Kim S, Nakayama A, Stott NE, Bawendi MG, Frangioni JV. Selection of quantum dot wavelengths for biomedical assays and imaging. Mol Imaging 2003;2:50–64. [PubMed: 12926237]
55. Ballou B, Lagerholm BC, Ernst LA, Bruchez MP, Waggoner AS. Non-invasive imaging of quantum dots in mice. Bioconjug Chem 2004;15:79–86. [PubMed: 14733586]
56. Larson DR, Zipfel WR, Williams RM, Clark SW, Bruchez MP, Wise FW, Webb WW. Water-soluble quantum dots for multiphoton fluorescence imaging in vivo. Science 2003;300:1434–1436. [PubMed: 12775841]
57. Wang HZ, Wang HY, Liang RQ, Ruan KC. Detection of tumor marker CA125 in ovarian carcinoma using quantum dots. Acta Biochim Biophys Sin (Shanghai) 2004;36:681–686. [PubMed: 15483748]

58. Voura EB, Jaiswal JK, Mattoussi H, Simon SM. Tracking metastatic tumor cell extravasation with quantum dot nanocrystals and fluorescence emission-scanning microscopy. Nat Med 2004;10:993–998. [PubMed: 15334072]

59. Kim S, Lim YT, Soltesz EG, De Grand AM, Lee J, Nakayama A, Parker JA, Mihaljevic T, Laurence RG, Dor DM, Cohn LH, Bawendi MG, Frangioni JV. Near-infrared fluorescent type II quantum dots for sentinel lymph node mapping. Nat Biotechnol 2004;22:93–97. [PubMed: 14661026]

60. Morgan NY, English S, Chen W, Chernomordik V, Russo A, Smith PD, Gandjbakhche A. Real time in vivo non-invasive optical imaging using near-infrared fluorescent quantum dots. Acad Radiol 2005;12:313–323. [PubMed: 15766692]

61. Dubertret B, Skourides P, Norris DJ, Noireaux V, Brivanlou AH, Libchaber A. In vivo imaging of quantum dots encapsulated in phospholipid micelles. Science 2002;298:1759–1762. [PubMed: 12459582]

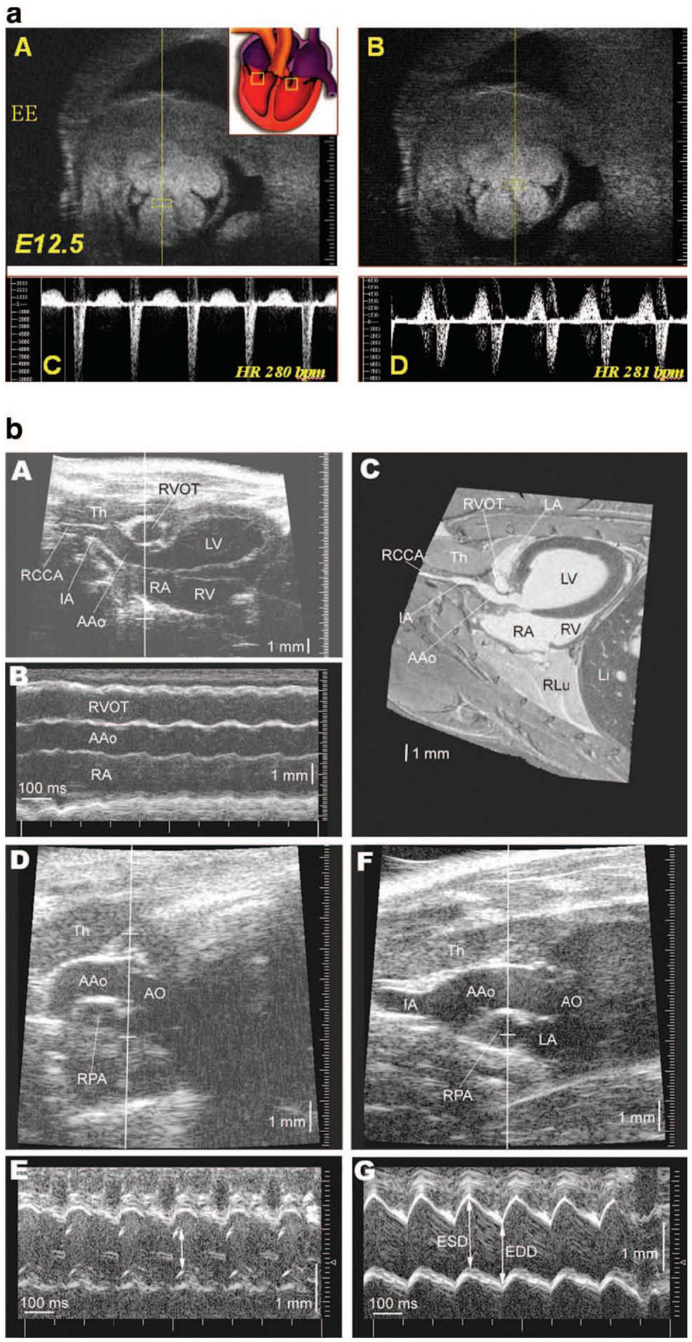

Figure 1.

A, View of embryonic mouse heart in utero at 12.5 days (A, B). The division of the inflow tract is visible. Yellow boxes in (A) and (B) show sample volume locations for Doppler flow spectra from mitral orifice in (C) and from tricuspid orifice in (D). The large tics on the right side of the image indicate a 1-mm scale. (Images courtesy of Dr. Stuart Foster.) B, Ultrasound biomicroscopy imaging of the left ventricular outflow tract and AAo, with anatomical confirmation from MR imaging in the mouse. A, UBM image of a left parasternal longitudinal section (LL2) showing the left ventricular outflow tract and AAo, as well as the RA and RV in the far field and the RVOT in the near field. B, M-mode recording simultaneously demonstrates the dimensional changes of RVOT, AAo, and RA through cardiac cycles. C, MR image of the similar section as for the UBM image in A. D, UBM image of a right parasternal longitudinal section (RL5) showing the AO and AAo, with M-mode cursor line across the aortic cusps. E, M-mode recording at the level of the AO showing the movement of the aortic cusps. The arrow indicates the opening of the aortic cusps during systole. F, UBM image of a right parasternal longitudinal section (RL5) showing the AO and AAo, but with the M-mode cursor line at the level of AAo. G, M-mode recording of the AAo showing the overall excursion and dimension changes through cardiac cycle. IA, innominate artery; RCCA, right common carotid artery; RVOT, right ventricular outflow tract; Th, thymus. (Figure reproduced with permission from Zhou et al.[21])

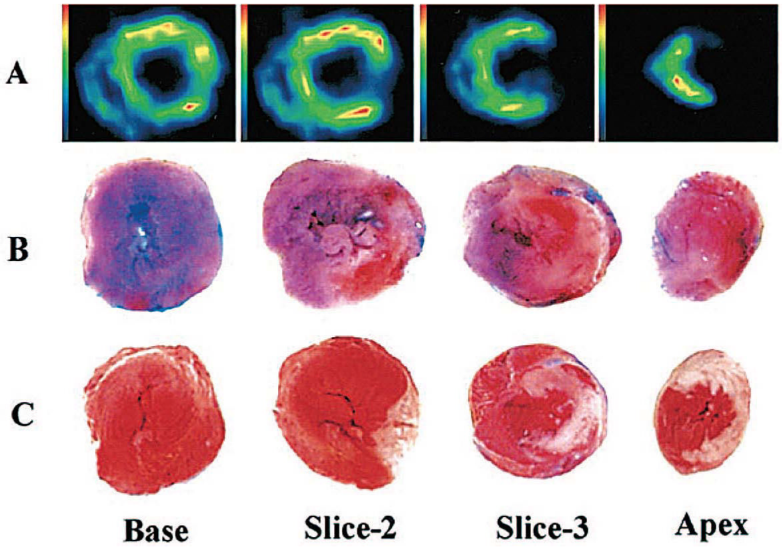

Figure 2.
Perfusion defects seen on in vivo FASTSPECT 99mTc-sestamibi images 2 hours after injection in the rat heart with ischemia-reperfusion (A) are consistent with myocardial ischemic area at risk, as determined by Evans blue dye (unstained by blue dye) (B), and with infarct myocardium, as determined by TTC staining (unstained by TTC) (C). (Figure reproduced with permission from Liu et al.[28])

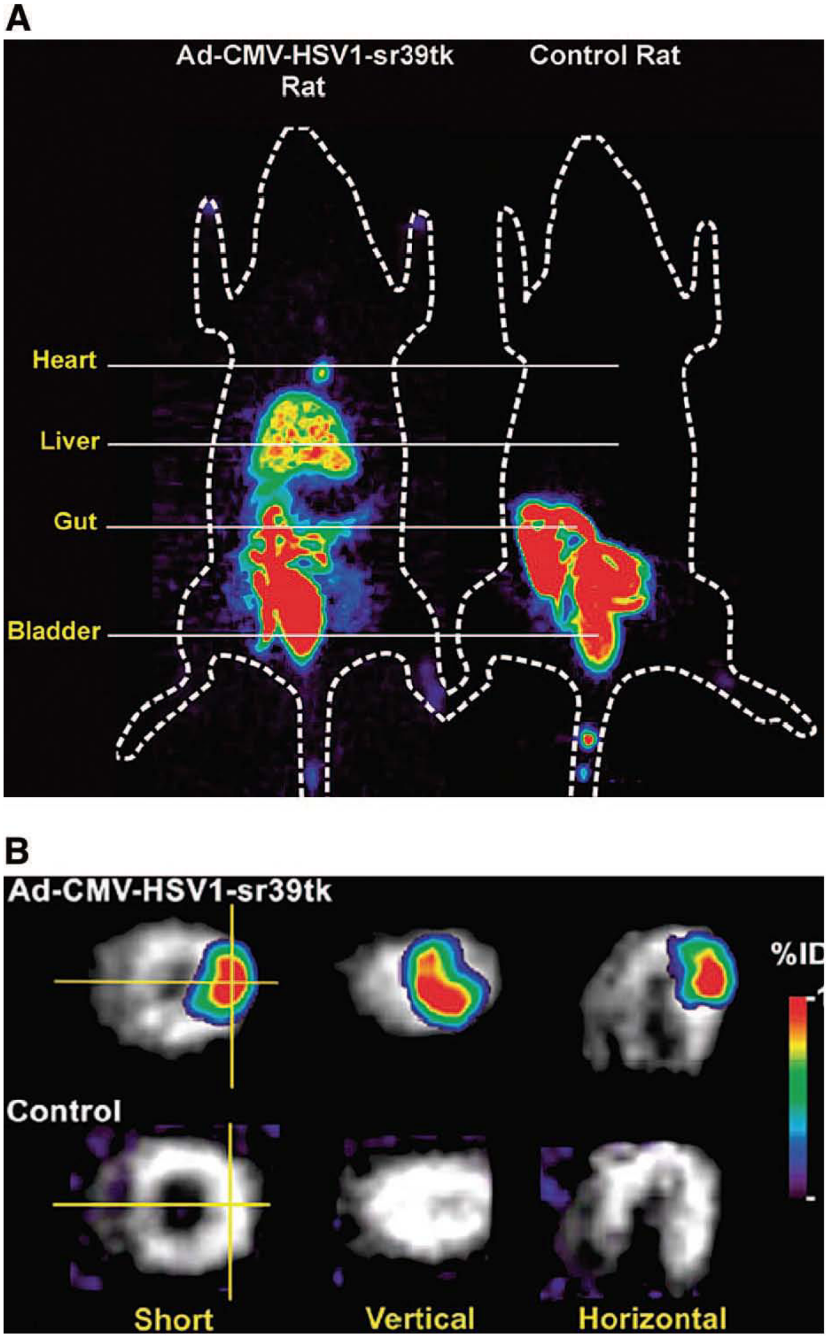

Figure 3.

These images show an example of imaging cardiac gene expression using adenoviral-mediated mutant thymidine kinase (HSV1-sr39tk) as a PET reporter gene expressed in the target cells and [18F]-FHBG as a PET reporter imaging probe. Trapping of tracer occurs only in cells expressing the reporter gene. A, At day 4, whole-body micro-PET image of a rat shows focal cardiac [18F]-FHBG activity at the site of intramyocardial Ad-CMV-HSV1-sr39tk injection. Liver [18F]-FHBG activity is also seen because of systemic adenoviral leakage with transduction of hepatocytes. Control rat injected with Ad-CMV-Fluc shows no [18F]-FHBG activity in either the cardiac of hepatic regions. Significant gut and bladder activities are seen for study and control rats because of route of [18F]-FHBG clearance. B, Tomographic views of cardiac microPET images. The [13N]-NH3 (gray scale) images of perfusion are superimposed on [18F]-FHBG images (color scale), demonstrating HSV1-sr39tk reporter gene expression. [18F]-FHBG activity is seen in the anterolateral wall for experimental rat compared with background signal in control rat. Perpendicular lines represent the axis for vertical and horizontal cuts. Color scale is expressed as % ID/g. (Figure reproduced with permission from Wu et al. *Circulation*. 2002;106:180–183.)

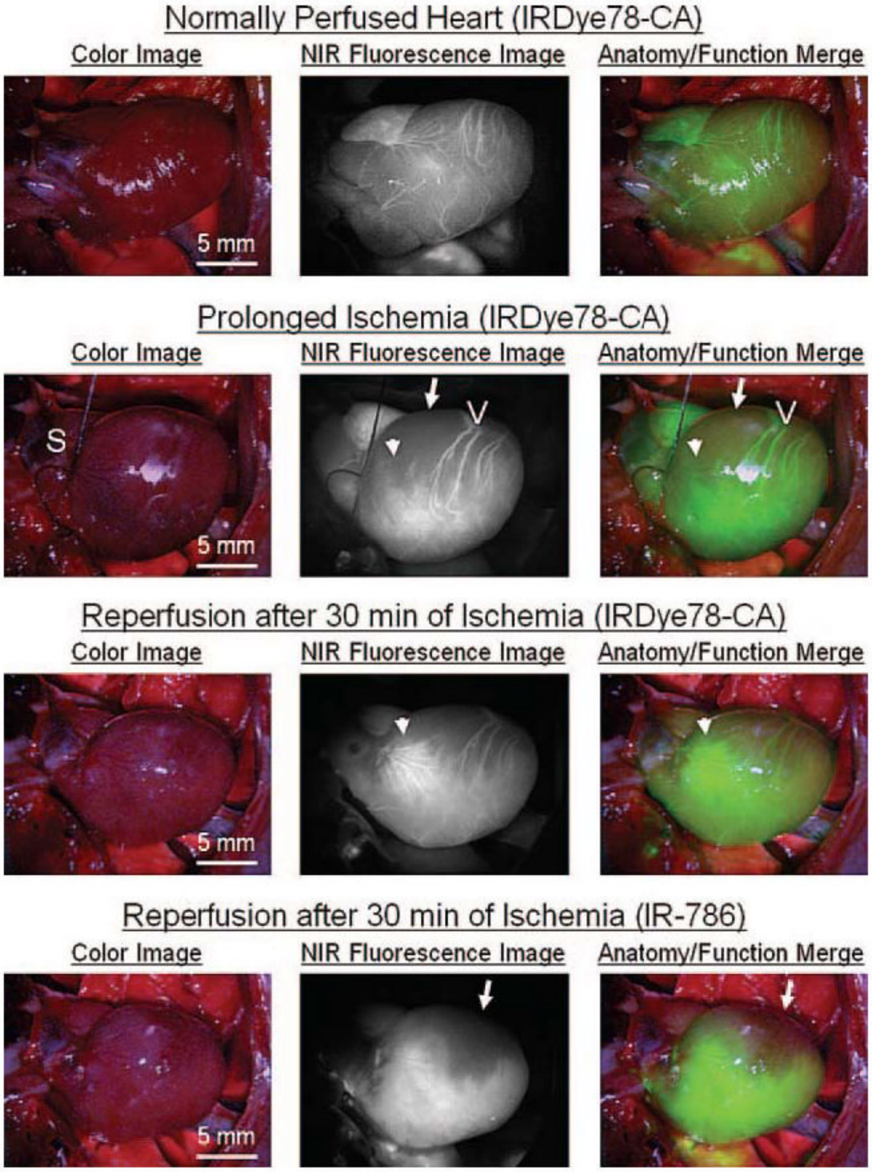

Figure 4.

Intraoperative NIR imaging of prolonged ischemia in the mouse heart. Normally perfused heart assessed with IRDye78-CA (top panels), after ligation of a branch of the LAD artery with a suture (S) and reinjection of IRDye78-CA (second panels). Occluded vessels (arrowheads), a blood flow defect (white arrows), and vascular engorgement (V) are now visible in the NIR fluorescence and pseudo-colored merged images. After a total of 30 minutes of ligation, removal of the suture and reinjection of IRDye78-CA (third panels), hyperemia of the previously ligated vessels is seen (white arrowheads). After injection of IR-786 (bottom panels), a large perfusion defect persists (white arrows). Data are representative of four independent experiments. (Figure reproduced with permission from Nakayama et al.[47])

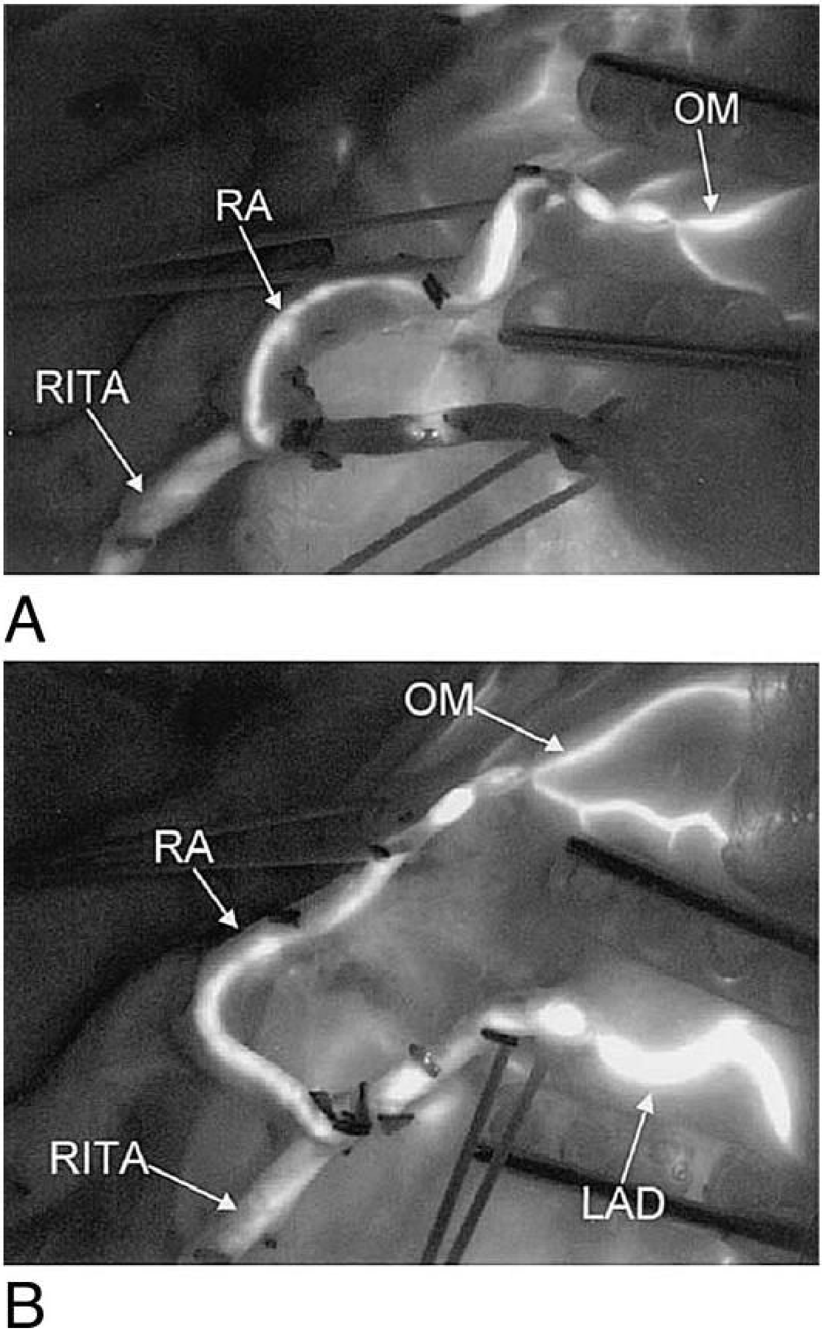

Figure 5.
A, A NIR fluorescence image showing in situ right internal thoracic artery (RITA) graft to the left anterior descending (LAD) coronary artery. A composite pedicled radial artery (RA) graft was placed from the RITA to the obtuse marginal artery. Note that no fluorescence was seen in the RITA distal to the RA anastomosis, which was taken down and reconstructed (seen in B). B, NIR fluorescence image taken after revision of RA-to-RITA anastomosis (seen in A). Note fluorescence now seen in distal portion of RITA graft and in LAD coronary artery. (OM, obtuse marginal coronary artery.) (Figure reproduced with permission from Taggart et al.[49])

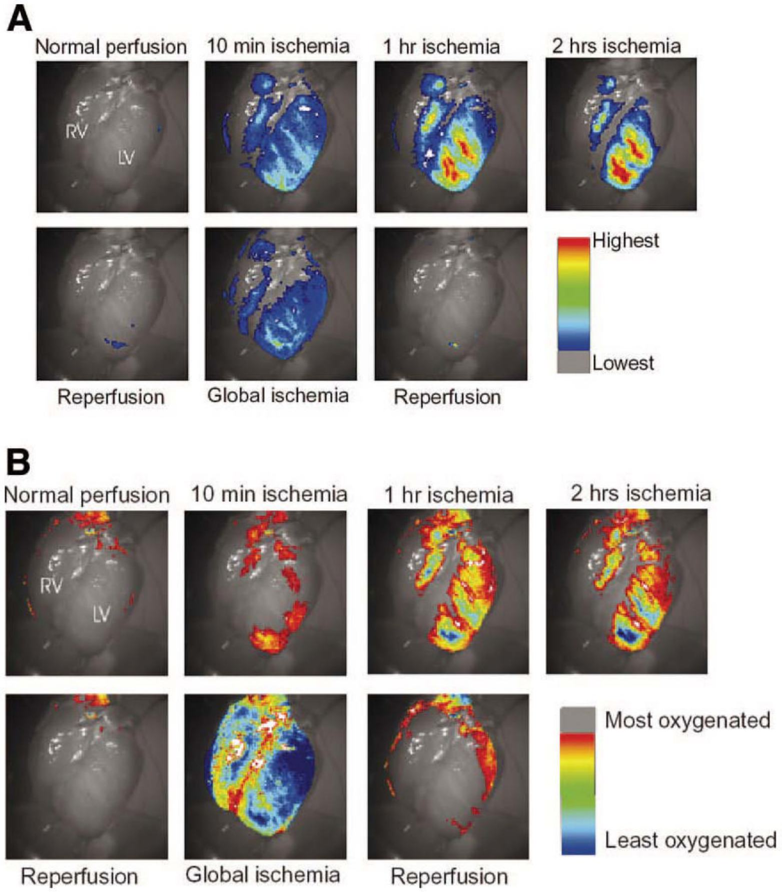

Figure 6.

A, Images showing the changes in deoxy-(Hb+Mb) concentration for the anterior side of the isolated pig heart during normal perfusion, LAD arterial occlusion and reperfusion. All color coded pixels have deoxy-(Hb+Mb) levels that are above those levels seen at normal perfusion on the left. For the color-coded pixels red indicates relatively higher deoxy-(Hb+Mb) levels than blue pixels. (Figure reproduced with permission from Nighswander-Rempel et al.[50]) B, Images showing the changes in oxy-(Hb+Mb) concentration for the anterior side of the isolated pig heart during normal perfusion, LAD arterial occlusion and reperfusion. All color-coded pixels have oxy-(Hb+Mb) levels that are below those levels seen at normal perfusion on the left. For the color-coded pixels red indicates relatively higher oxy-(Hb+Mb) levels than blue pixels. (Figure reproduced with permission from Nighswander-Rempel et al.[50])

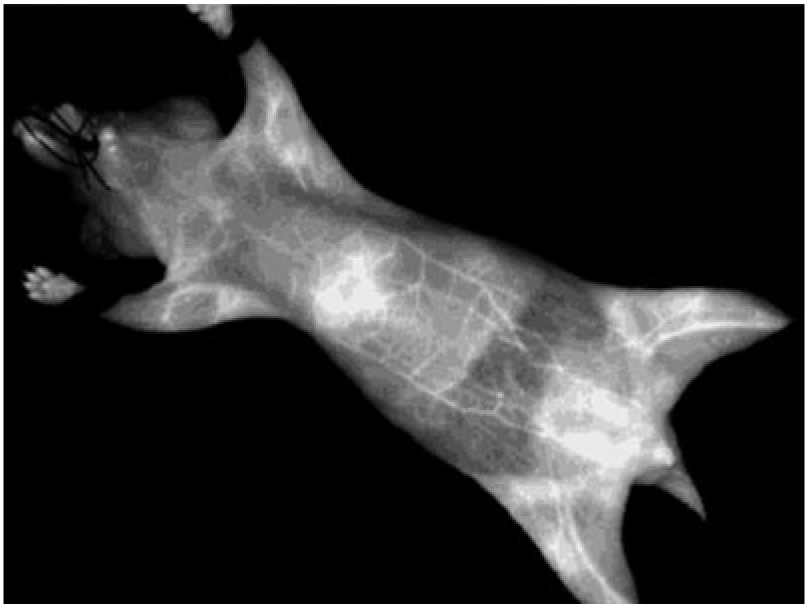

Figure 7.
A noninvasive angiogram of a nude mouse one minute after injection of 645-nm quantum dots conjugated to polyethylene glycol amine. Excellent vascular contrast and liver uptake is visible. (Figure reproduced with permission from B. Ballou et al.[55])

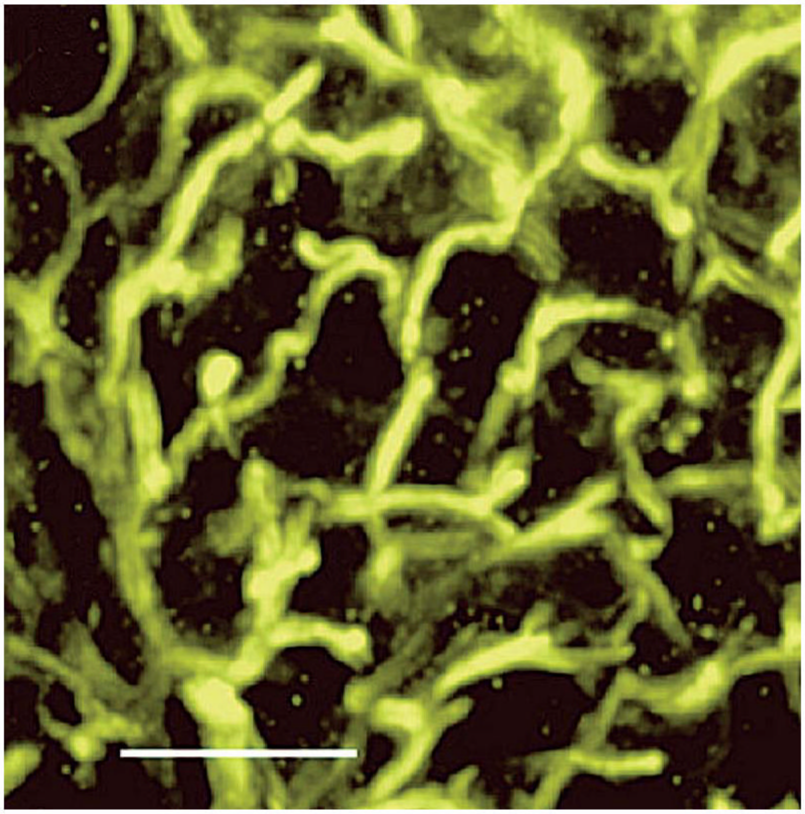

Figure 8.

In vivo two-photon imaging of vasculature labeled by a tail vein injection of water-soluble QDs (fluorescence wavelength, 550 nm; TEM diameter, 4.3 nm, excitation 780 nm). This image shows a projection of capillary structure through 250 μm of adipose tissue (50 images, 5 μm per step). The scale bar represents 50 μm. (Figure reproduced with permission from D. R. Larson et al. *Science* 2004;300:1434.)